Applied Catalysis B: Environmental 250 (2019) 369–381

Contents lists available at ScienceDirect

Applied Catalysis B: Environmental

journal homepage: www.elsevier.com/locate/apcatb

MOF-derived hollow TiO_2@C/$FeTiO_3$ nanoparticles as photoanodes with enhanced full spectrum light PEC activities

Jian Wang[a,b], Chuang Xue[a], Wenqing Yao[b,*], Jun Liu[c], Xingxing Gao[d], Ruilong Zong[b], Zhuang Yang[a,b], Wenjie Jin[e], Dongping Tao[a]

[a] School of Mining Engineering, University of Science and Technology Liaoning, Anshan 114051, Liaoning Province, PR China
[b] Department of Chemistry, Tsinghua University, Beijing 100084, PR China
[c] School of Materials Science of Technology, South China University of Technology, Guangzhou 510641, PR China
[d] School of Civil Engineering, University of Science and Technology Liaoning, Anshan 114051, Liaoning Province, PR China
[e] School of Chemical Engineering, University of Science and Technology Liaoning, Anshan 114051, Liaoning Province, PR China

ARTICLE INFO

Keywords:
Ilmenite $FeTiO_3$
Metal-organic frameworks
Photoelectrocatalysis
Full spectrum light

ABSTRACT

In the current work, the ternary TiO_2@C/$FeTiO_3$ (TCF) hollow nanotubes are synthesized using MOF-Fe nanorods as a sacrificial template and precursor via the thermal carbonization under N_2 atmospheres. Due to such delicate structure features that consist of hollow needle-like framework, middle conductive-layer carbon and monodisperse $FeTiO_3$ nanoparticles embedded on carbon layer, the hollow TCF composites can effectively harvest full spectrum light energy, enhance the interfacial charge separation and suppressed the recombination of photogenerated electron-hole pairs, resulting in enhanced photoelectrocatalytic (PEC) activity. Among as-synthesized samples, TCF-20% photoanode exhibits the best performance towards the degradation of phenol under full spectrum light irradiation with an anodic bias of 1.5 V vs. SCE and the degradation rate constant is 0.586 h^{-1}, which is 2.75 times larger than that of the corresponding sum of both EC and PC process. In addition, triple synergistic effects of the possible mechanism with the enhancement of PEC activity was proposed on the basis of PEC degradation results. This work also opens a new insight for synthesis of photocatalysts based on novel MOFs.

1. Introduction

With two major problems of serious environmental pollution and depletion of fossil fuel resources, photocatalysts have drawn more considerable interest due to its advantages including naturalness, safety, cleanness and renewable source of energy [1–4]. Unfortunately, the photocatalytic activities of currently developed photocatalysts are far from practical application because of its low utilization of solar energy and low separation efficiency of photo-induced electron-hole pairs [5–7]. Therefore, it is a crucial issue for developing a low-cost, highly efficient, sustainable, and environmentally friendly photocatalysts by designing novel materials or various structures.

In recent years, metal-organic-frameworks (MOFs) have been paid much attention due to their ultrahigh porosity, a large surface area and structural tenability [8–10]. MOFs are highly crystalline and porous hybrid materials composed of inorganic metal clusters as network nodes and organic ligands as linkers, and have been applied in many fields, such as gas storage, molecule separation, lithium batteries, drug delivery and catalysis [11,12]. In addition to direct use, MOFs has also been used as self-sacrificial templates and precursors to synthesize MOF-derived porous heterostructures by a simple solid-state thermal treatment under controlled atmospheres, such as $NiFe_2O_4/Fe_2O_3$ [13], $ZnO/ZnFe_2O_4$/C [14] and Co_3O_4/TiO_2 [15]. Comparing with other templates, MOFs exhibited novel properties because of their unique structure, high specific surface area, and controlled porosity [16–18]. Although MOFs as templates for porous metal oxide/carbon matrix composites have been employed on electrode materials such as lithium batteries [19], there are a few reports on using MOFs as the self-sacrificial templates and precursors to synthesize MOF-derived photocatalysts with well-defined morphology. If immobilization of nanoparticles on porous carbon supports via thermal carbonization of MOFs templates, the consequent MOF-derived metal oxide/carbon matrix composites can exhibit distinct merits by the multi-component of metal oxide, porous carbon and metallic nanoparticles with a desired structural features, which can enhance photoelectrocatalytic (PEC) performance in terms of high electrical conductivity and electrochemical

* Corresponding author.
E-mail address: yaowq@mail.tsinghua.edu.cn (W. Yao).

https://doi.org/10.1016/j.apcatb.2019.03.002
Received 21 October 2018; Received in revised form 3 February 2019; Accepted 1 March 2019
Available online 02 March 2019
0926-3373/

activity.

On the other hand, TiO_2-based heterojunction composites have been widely studied due to enhanced the photocatalytic ability for building an internal electrostatic potential in the heterojunction interface, which can suppress the electron-hole pair recombination, enhance the efficiency of interfacial charge transfer and harvest light absorption [20–25]. Inspired by these advantages, coupling $FeTiO_3$ with TiO_2 forming the high compatible $FeTiO_3$-TiO_2 heterostructure have attracted much attention owing to excellent performance of photocatalytic activity. For example, Wan In Lee et al. synthesized $FeTiO_3$/TiO_2 heterojunction-type photocatalyst with the enhancement of visible-light photocatalytic degradation of organic compounds [26]. More recently, Fu et al. reported that an effective water oxidation catalyst of hierarchical $FeTiO_3$-TiO_2 hollow spheres are prepared via a two-step sequential solvothermal process and followed by thermal treatment [27]. Truong et al. used a facile hydrothermal method to synthesize a uniform heterojunction photocatalyst of $FeTiO_3$/TiO_2 composites, and it exhibits remarkable photocatalytic activity on CO_2 reduction to CH_3OH under both visible and UV–vis light irradiation [28]. However, the controllable morphology and structure of $FeTiO_3$/TiO_2 composites are of great fundamental importance and major challenge for the complexity of the strong interactions between two components heterojunction and their influence on the phtotocatalytic activities. Moreover, up to now there is still a few research works on the utilization of MOFs as sacrificial templates and precursors to synthesized complicated ternary TiO_2@C/$FeTiO_3$ heterostructure composites with desirable PEC properties in accurately controllable compositions and morphologies.

Herein, the ternary hollow TiO_2@C/$FeTiO_3$ (abbreviation TCF) heterostructures nanocomposites have been rationally designed and synthesized using Fe-MOF nanorods as sacrificial templates and precursors by a simple calcining process of amorphous TiO_2 coating Fe-MOF nanorods. More specially, in comparison with previous study, hollow TCF nanocomposites demonstrate a novel structure, which TiO_2 layer were deposited onto the surface of the $FeTiO_3$-embedded carbon layer. The obtained hollow TCF composites photoanodes exhibited enhanced photoelectrocatalytic (PEC) activity towards the degradation of phenol with excellent stability under full spectrum light irradiation. Furthermore, a possible full spectrum light induced mechanism for the PEC degradation of phenol is proposed by integrating synergistic effects of wide spectrum absorption, delicate structure features and electro-oxidation assisted photocatalysis.

2. Experimental

2.1. Synthesis of Fe-MOFs nanorods

All chemicals used were reagent grade and used without any further treatment. Fe-MOFs (MIL-88-Fe, $Fe_3O(H_2O)Cl(BDC)_3.nH_2O$) was synthesized by a simple solvothermal method according to the ever reported literature with a modified procedure [29]. Typically, $FeCl_3.6H_2O$ (0.004 mmol) and 1,4-benzenedicarboxylic acid (1,4-H_2BDC acid 0.006 mmol) was added into 60 mL mixed *N,N*-dimethylformamide (DMF) and ethanol (4:1 vol ratio) solution under vigorous stirring for 1 h at room temperature. Subsequently, the mixture was transferred to a 100 mL Teflon-lined stainless steel autoclave and maintained at 120 °C for 24 h. Finally, the obtained pale yellow precipitates were collected by centrifugation, washing with DMF and ethanol three times respectively, and drying over-night in vacuum oven at 80 °C.

2.2. Preparation of TiO_2@C/$FeTiO_3$ (abbreviation TCF) nanotubes photocatalysts

Different amount Fe-MOFs ($Fe_3O(H_2O)Cl(BDC)_3.nH_2O$) nanorods (0.098, 0.147, 0.196, 0.245 mmol) were dispersed into 60 mL of anhydrous ethanol solution and mixed with 0.3 ml of $NH_3.H_2O$ (28%) under sonication to form uniform suspension. Subsequently, 1 ml (2.938 mmol) tetrabutyl titanate (TBOT) was added to the above suspension drop by drop under vigorous stirring, and the reaction is kept at 45 °C for 18 h. Then, the obtained TiO_2@Fe-MOFs samples were washed thoroughly with ethanol, followed by drying under vacuum at 80 °C overnight. Finally, TiO_2@Fe-MOFs samples were heated in a quartz tube to 600 °C in N_2 atmosphere at a ramping rate of 5 °C min^{-1} and kept at this temperature for 5 h to obtain the respective hollow TCF composites with different molar ratio of Fe/Ti (10, 15, 20, 25%), which were denoted as TCF-10%, TCF-15%, TCF-20%, TCF-25%, respectively. For comparison, TiO_2 nanoparticles were obtained by the directly annealing of hydrolysis samples of TBOT under the same condition described above. SEM images of TiO_2 nanospheres were shown in Fig. S1. In order to prove the effect of carbon, TiO_2@$FeTiO_3$-20% (Fe/Ti) nanotubes photocatalysts have been synthesized under the same condition described above, except for the calcination in the air. FESEM images and TEM images of TiO_2@$FeTiO_3$-20% was shown in Fig. S2 and Fig. S3.

2.3. Fabrication of the TiO_2@C/$FeTiO_3$ film electrodes

The TCF film electrodes were prepared by a dip-coating method proposed by our precious reports [30,31]. Typically, TCF composites (50 mg) were added into 200 mL of water solution by ultrasonic for 6 h at room temperature. Subsequently, the indium-tin oxide (ITO) glass (width 20 × length 40 mm, 1.1 mm thickness and a sheet resistance 15Ω/square) was immersed vertically into the above-mentioned TCF suspension and the parameters in the process of dip coating were adopted as listed below: hoisting height: 35 mm, lifting speed: 50 μm/s, residence time: 30 s, immersion time: 60 s, the number of repetitions: 3 times. Moreover, the prepared film electrodes were dried at 80 ℃ for 30 min under nitrogen protection after dipping every time. Fig. S4 shows the typical top-view and cross-sectional FESEM images of TCF-20% film electrodes.

2.4. Characterization of TiO_2@C/$FeTiO_3$ photocatalysts

The prepared TCF samples were characterized by X-ray diffractometry (XRD) measurement (Bruker D8 Advance X-ray diffractometer, Cu Kα (λ = 1.5406 Å). The morphology and structure of as-synthesized obvious TCF samples were performed by transmission electron microscopy (TEM, JEM 2010 F) and field emission gun scanning electron microscope (FESEM, Hitachi SU-8010), respectively. The UV–vis diffuse reflectance spectra (DRS) of the samples were measured using Hitachi UV-3010 spectrophotometer and $BaSO_4$ was used as a reference for baseline correction. The content of carbon in TCF composites were investigated by TGA/DSC (Mettler Toledo TGA/DSC 1) at a heating rate of 10 ℃/min. Raman spectra were measured on HORIBA HR800 Raman spectrometer. PHI Quantera system (USA) was used to get XPS spectra. Fourier transform infrared (FTIR) spectra were collected using Bruker V70 spectrometer. Photoluminescence (PL) spectra were acquired at room temperature using a JASCO FP-6500 with an excitation wavelength of 375 nm. The electron spinresonance (ESR) signals of radicals was obtained on a Bruker model ESR JES-FA200 spectrometer. Total organic carbon analyzer (Jena AG) was used to evaluate the mineralization degree analysis of the phenol solution. Photoelectrochemical measurements were recorded on a three-electrode electrochemical system (CHI-660D, China).

2.5. Photoelectrochemical (PEC) degradation of phenol

Photoelectrochemical (PEC) degradation of phenol was investigated on an electrochemical workstation (CHI 660 B) with a three-electrode cell, which consists of Pt wire as a counter electrode, saturated calomel electrode (SCE) as reference electrodes, and TCF films electrodes as the

working electrode (photoactive area of 6 cm^2), respectively. The quartz reactive cell (50 width × 50 lengths × 100 height mm) which put into 100 mL mixed aqueous solution with a concentration of 0.1 M Na_2SO_4 as the supporting electrolyte and 5 ppm phenol as target contaminant, paralleled with 500 W xenon lamp (CHF-500 produced in Beijing Changtuo Technology Co., Ltd), which was used directly without any filter as the full spectrum light source (320–2500 nm), and was located at a distance of 10 cm away from the light source. The positive potential (1.5 V) was applied to the TCF films electrodes through an electrochemical system (CHI-660D, China). Before irradiation, dark experiments were performed for 30 min under vigorous stirring to achieve absorption-desorption equilibrium. Every time intervals during the PEC degradation process, 3 mL of the reactive phenol solution was sampled to analyze the concentration of phenol and its intermediate products using an HPLC (high performance liquid chromatography) system equipped with an UV–vis K2501 detector, a Venusil XBP-C_{18} column (Agela Technologies Inc.) and an auto-sampler (20 vial capacity with 6-line degasser channels).

3. Results and discussion

Scheme 1 illustrates the detailed fabrication process of uniform hollow TCF nanotubes. First, the sacrificial template of Fe-MOFs (MIL-88-Fe, $Fe_3O(H_2O)Cl(BDC)_3.nH_2O$) nanorods were facilely synthesized by a solvothermal method using $FeCl_3.6H_2O$ and 1,4-benzenedicarboxylic acid (1,4-H_2BDC acid) as reactant in a *N,N*-dimethylformanmide (DMF) solution [32]. During the solvothermal process, metal Fe^{3+} ions having their open coordinated sites can coordinate carboxylate group of 1,4-H_2BDC acid by strong metal-ligand bonds to form a crystalline highly porous Fe-MOFs nanorods. The as-synthesized Fe-MOFs nanorods were added into anhydrous ethanol solution under sonication and then, tetrabutyl titanate (TBOT) was added to the above suspension in the presence of $NH_3.H_2O$. A subsequent low temperature pyrolysis of TBOT has resulted in a homogeneously amorphous TiO_2 layer coating the surface of Fe-MOFs nanorods to obtain core-shell TiO_2@Fe-MOFs nanorods. Finally, hollow TCF nanotubes have been obtained via the calcination of these TiO_2@Fe-MOFs nanorods precursors at 600 °C for 5 h in N_2 atmosphere. In the calcination process, Fe-MOFs nanorods have been transformed hollow nanotubes due to the carbonization of organic complex Fe-MOFs. At the same time, Fe^{3+} ions were converted to Fe^{2+} through carbonization-induced carbothermal reduction and reacted with TiO_2 via in situ solid state reaction to form $FeTiO_3$ nanoparticles on the inner surface of carbon layer. This conversion process has resulted in a novel structure of hollow TCF composites, which TiO_2 layer were deposited onto the surface of the $FeTiO_3$-embedded carbon layer.

The morphology and microstructure characterization of as-synthesized Fe-MOFs nanorods and TCF hollow nanotubes with the different molar ratio (Fe/Ti) are observed by FESEM at different magnifications. As shown in Fig. 1a–c, as-synthesized Fe-MOFs samples exhibited a uniform needle-like nanorod morphology, which is relatively smooth with an average diameter of 140 nm and a length of about 600 nm. The FESEM images of Fig. S5 shows the morphologies of TCF samples which the molar ratio of Fe:Ti is 0.5%, 1%, 3%, 5% and 10%, respectively. From the abovementioned observations in Fig. S5, it clearly indicates that the Fe-MOFs nanorods play the role of sacrificial template, and provide framework to guide the hydrolysis reaction of TBOT and coating of TiO_2. Moreover, the molar ratio of Fe/Ti have a great influence on the phase and morphology of as-synthesized TCF samples. However, when the molar ratio of Fe/Ti was increased to 15%, a large number of TCF nanotubes (Fig. 1d) with a high production of more than 90% can be observed. After the calcination of core-shell TiO_2@Fe-MOFs in N_2 atmosphere, as-synthesized TCF nanotubes still remains the overall rod-shape but coarse and porous surface composed of TiO_2 are observed, which results from gas evolution from the thermal carbonization of organic linkers. After coating TiO_2 layers, 15%-TCF nanorods are about 600–700 nm in length and 160 nm in diameter, as shown in Fig. 1e and f. As displayed in Fig. 1g–l, as-synthesized TCF-20% and TCF-25% samples well retained uniform nanorod structure and the average diameters were about 155 and 150 nm, respectively. The magnified FESEM images shows that the broken TCF nanotubes with different molar ratio Fe/Ti (15%, 20% and 25%) appear transparent hollow structured interiors which is shown the red circles in Fig. 1e, h, k and l. It should be noted that although the diameter of TCF nanotubes with the molar ratio of Fe/Ti (15%, 20% and 25%) is slightly larger than that of Fe-MOFs nanorods due to the coating of TiO_2, the diameter of TCF nanotubes become more and more smaller and the aspect ratio of TCF nanotubes gradually increased with the increasing of molar ratio of Fe/Ti, indicating that TiO_2 layer covers on the surface of Fe-MOFs nanorods support, and the coating process undergoes from the sufficient amount to excessive amount of Fe-MOFs nanorods. It can be inferred that the molar ratio of Fe/Ti can control the coating thickness of TiO_2 shell to some extent, causing opportunities to adjust their structure-related properties. Moreover, EDX mapping for TCF nanotubes with the molar ratio of Fe/Ti (15%, 20% and 25%) were shown in Fig. S6.

To explore the detailed morphology and structure of the as-obtained samples, TEM and HRTEM was further performed. As shown in Fig. 2, TCF nanotubes with the molar ratio of Fe/Ti (15%, 20% and 25%) exhibited a well-ordered hollow needle-like nanostructures for conspicuous color contrasts of dark and bright regions between the central and outer edge areas of the TCF nanotubes, which is well in agreement with the results of the FESEM images. The outer surface of TCF nanotubes with the molar ratio of Fe/Ti (15%, 20% and 25%) became

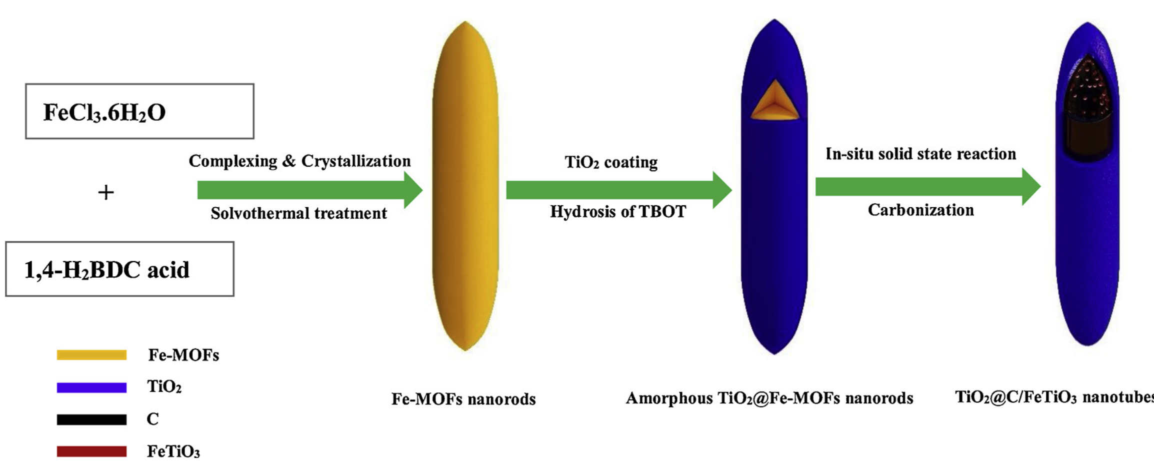

Scheme 1. Detailed formation process hollow TCF nanotubes.

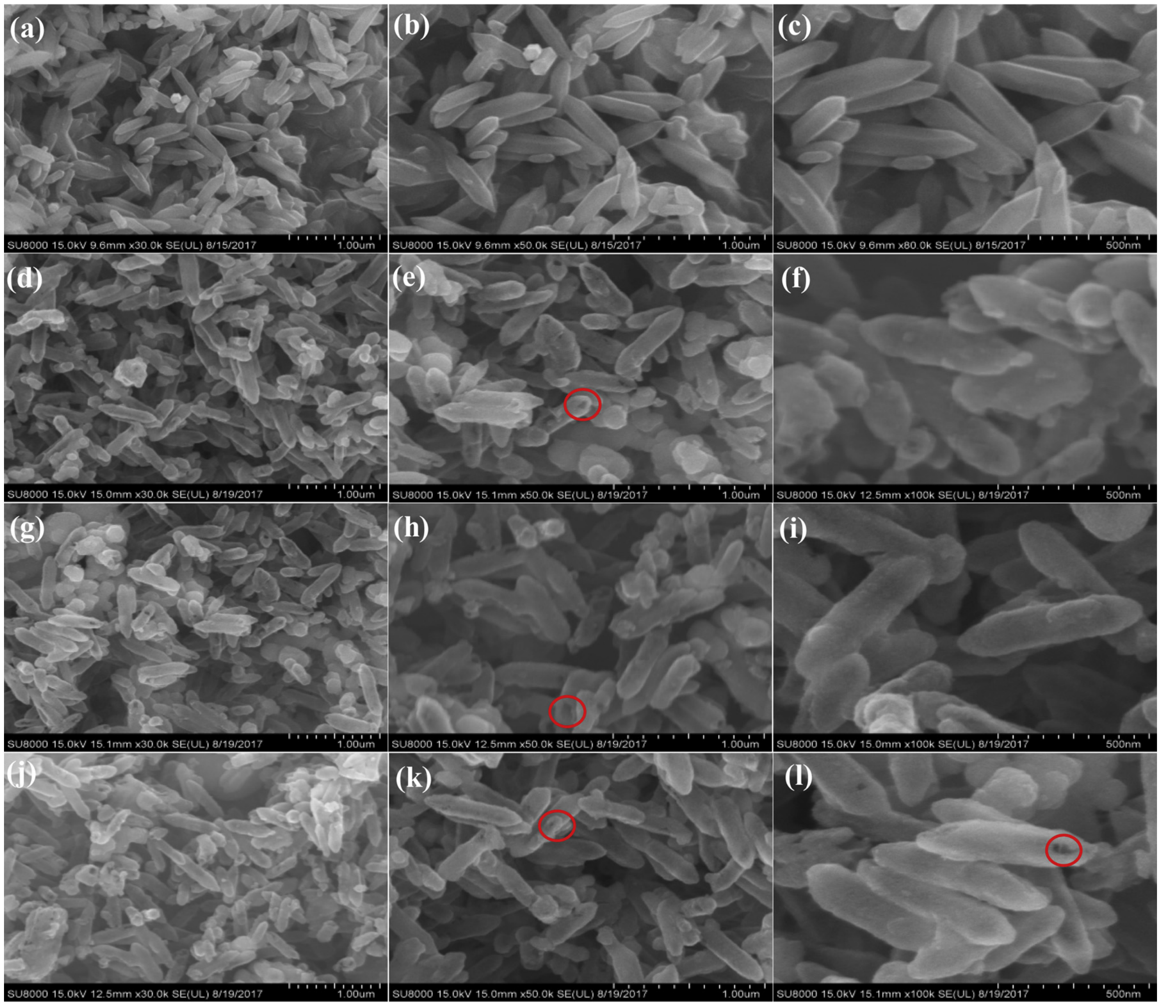

Fig. 1. (a–c) Low- and high-magnification FESEM images of Fe-MOFs nanorods. (d–f) FESEM images of a typical TCF-15% nanotubes showing the well-defined nanorod morphology. (g–i) FESEM images of TCF-20% nanotubes, displaying their hollow structure features. (j–l) FESEM images of TCF-25% nanotubes.

relatively rough due to sol-gel synthesis of TiO_2 tightly coated onto the surface of carbon layer and the evident wall thickness of TCF nanotubes was approximately determined to be about 25, 22 and 20 nm (Fig. b, h and n), respectively. Moreover, close observation of HRTEM images (Fig. 2j–l, p and q) proved that $FeTiO_3$ nanoparticles with a grain size range of 5–10 nm were decorated into the thin inner layer of carbon layer, while a few of $FeTiO_3$ nanoparticles distribute internal or external regions of nanotubes. It is of great significance that $FeTiO_3$ nanoparticles firmly embedded on the carbon layer without any aggregation, which could significantly enhance the adhesion with carbon layer utilizing a bonding effect via in situ solid state reaction. With increasing the molar ratio of Fe/Ti (15%, 20% and 25%), although the grain size of the $FeTiO_3$ does not obviously change, wall thickness of TiO_2 decreases a little lower, indicating that the wall thickness of TiO_2 can be controllably tuned within a certain range by changing the kinetics of hydrolysis and condensation of the amount of TBOT, creating opportunities to regulate structural features related properties. This exquisite nanostructure was caused via the in situ solid state reaction of formation of $FeTiO_3$ and carbon layer due to the carbonization of organic BDC ligands. As seen in HRTEM images of Fig. 2c–f, i–l and o–r, the lattice spacing of 0.250 nm and 0.325 nm corresponded to (101) and (110) planes of anatase TiO_2, respectively, while the clear interplanar distance of 0.272 nm is consistent with the lattice spacing of (104) lattice plane of rhombohedral-phase $FeTiO_3$, suggesting good crystallinity. The composites TCF nanotubes have exhibited delicate structure features, such as hollow needle-like framework, middle conductive-layer C and monodisperse $FeTiO_3$ nanoparticles embedded on carbon layer, which might enhance the interfacial charge separation.

The elemental composition and distribution status of the as-synthesized TCF-20% nanotubes were further characterized by Energy-dispersive X-ray spectroscopy (EDS) elemental mapping measurements (Fig. 3). Fig. 3a shows the dark-field TEM image of TCF-20% nanotubes, displaying hollow nanotubes with an average wall thickness of 22 nm and uniform inner diameter of 100 nm, and the spatial distribution of $FeTiO_3$ nanoparticles with a size distribution of 5–10 nm, which was decorated on the inter carbon layer. The EDS elemental mapping analysis (Fig. 3b-e) confirmed that Fe (Fig. 3b), C (Fig. 3c), Ti (Fig. 3d), and O (Fig. 3e) elements present in the hollow TCF-20% nanotubes. As a comparison, Ti and O atoms which exhibit strong signals, were distributed over the entire hollow framework, suggesting TiO_2 shell uniformly coated on the outer layer of TCF composites and TiO_2 inner layer attached to carbon layer, and whereas Fe atoms which exhibit weak signals, were mainly located in the shell region only, suggesting that most of $FeTiO_3$ nanoparticles were decorated on the carbon layer. Moreover, the overlapped image (Fig. 3f) of Fe, Ti, C and O elements agreed well with the TEM image in Fig. 2g and also provided remarkable evidence for hollow structure with elemental dots sparsely distributed in the middle of the blank part of TCF-20% nanotubes.

To further investigate the crystalline structure of the TCF nanotubes with the different molar ratios of Fe/Ti, XRD patterns were recorded in Fig. 4a. Once the TiO_2 shell was coated on the Fe-MOFs nanorods and calcined in N_2 atmosphere, all TCF (10%, 15% and 25%) nanotubes

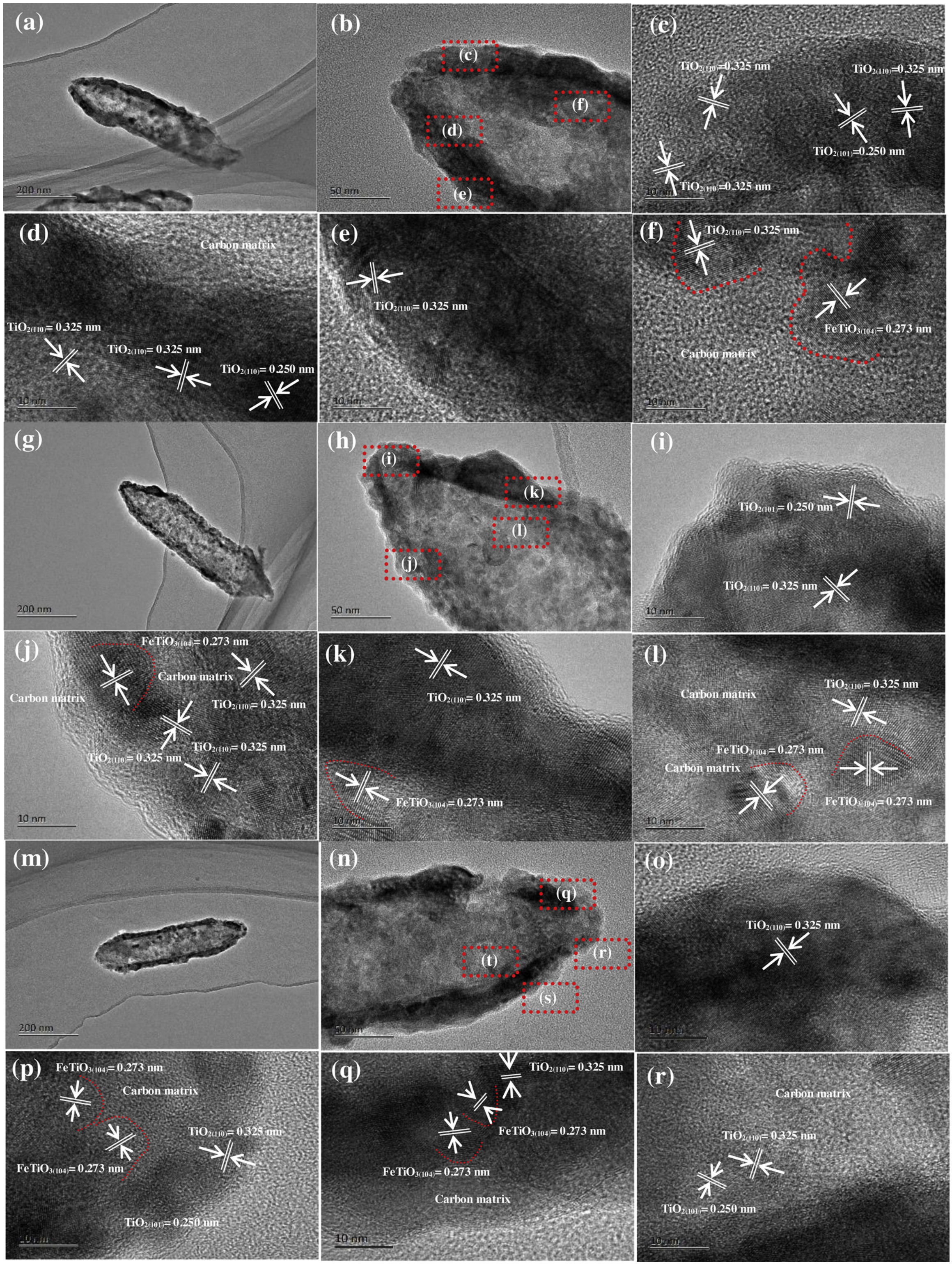

Fig. 2. TEM and HRTEM images of TCF nanotubes with the various molar ratio of Fe/Ti (15%, 20% and 25%): (a–f) TCF-15% nanotubes; (g–l) TCF-20% nanotubes; (m–r) TCF-25% nanotubes.

present three sets of X-ray diffraction peaks, which can be indexed to the rhombohedral $FeTiO_3$ (JCPDS no. 29-733), tetragonal phase TiO_2 (JCPDFS no. 71-650) and rhombohedral carbon (JCPDS no. 75-444), respectively. Moreover, the diffraction peaks with 2θ values of 23.9°, 32.6°, 35.5°, 40.5°, 48.9°, 61.9°, 63.4° corresponded to (012), (104), (110), (113), (018), (124), (300) crystal faces of rhombohedral structure of $FeTiO_3$ (JCPDS no. 29-733), whereas the diffraction peaks at 27.3°, 35.9°, 41.2°, 54.1°, 56.2°can be attributed to the (110), (101), (111), (211), (220) crystal planes of anatase TiO_2 (JCPDFS no. 71-650) and the diffraction peaks at 25.3°can be indexed to (111) crystal planes of rhombohedral carbon (JCPDS no. 75-444). Moreover, the diffraction peaks of (110) and (113) crystal planes of $FeTiO_3$ are very close to the peaks of the (101) and (111) crystal planes of TiO_2, the peaks overlapped and broadened. With the increasing of molar ratio of Fe/Ti from

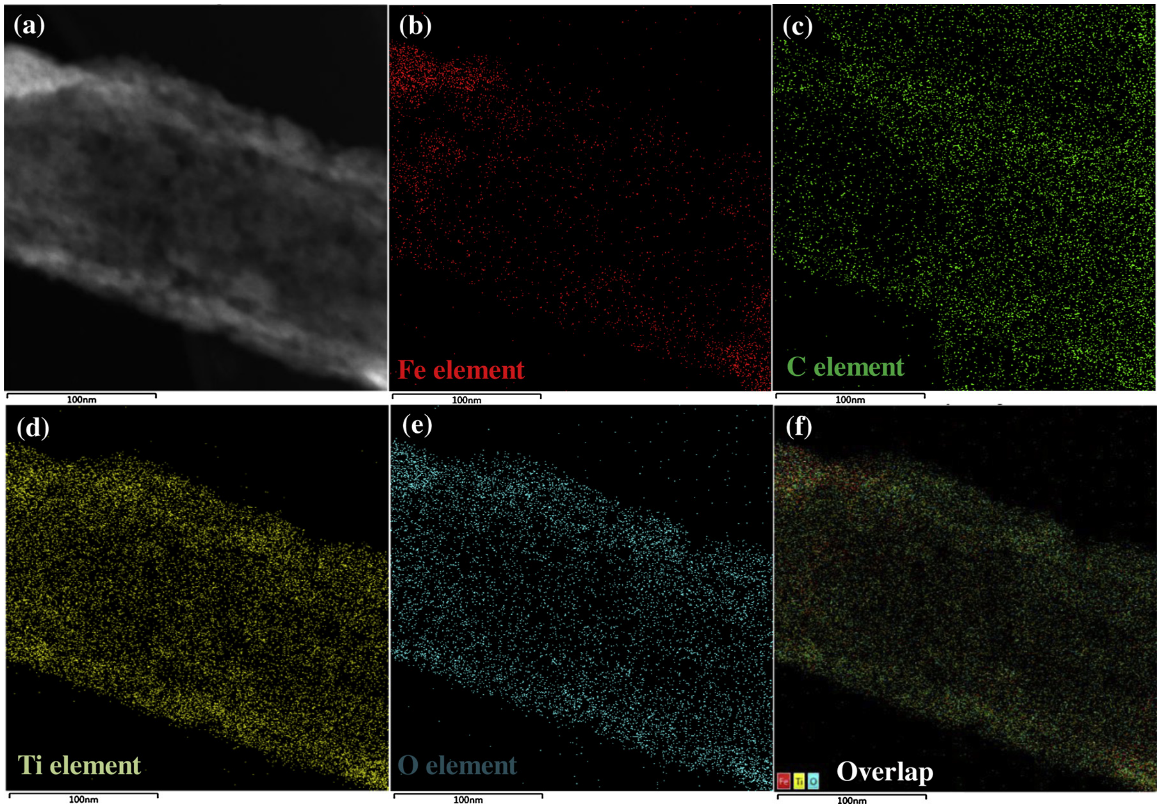

Fig. 3. Dark-field TEM images of TCF-20% nanotubes showing that $FeTiO_3$ nanoparticles decorated on the carbon layer and the corresponding EDS elemental mapping of (b) Fe, (c) C, (d) Ti, (e) O and (f) all components.

10% to 25%, the intensity of the $FeTiO_3$ and carbon diffraction peaks gradually increased, while the peak intensities of TiO_2 apparently weakened, indicating the successful conversion of TiO_2@Fe-MOF composites into TCF composites via *in situ* solid state reaction. Notably, compared to the standard pattern of rhombohedral carbon (JCPDS no. 75-444), the peak of (111) plane shifted low degree due to crystalline lattice mismatch between $FeTiO_3$ and carbon layer.

To further calculate the amount of carbon mass content in these TCF composites, thermogravimetric analysis (TGA) was carried out from room temperature to 700 °C under air at heating rate of 10 °C min^{-1}. It can be seen from Fig. 4b that TCF composites with different molar ratio Fe/Ti has occurred to weight loss in two major temperature regions. The first stage of small weight loss can be attributed to the removal of physically adsorbed water in the temperature range 80–130 °C. In the second stage, there is a rapid mass loss from 350 to 550 °C for TCF composites, which is caused by the release of CO_2 from the combustion of some carbon layer in the TCF composites. As revealed by TGA results, the carbon content was determined to be 10.67%, 13.12%, 14.18% and 16.42% for TCF-10%, TCF -15%, TCF -20% and TCF -25%, respectively. The structural characteristics of the TCF composites were further analyzed by FTIR spectra and Raman spectroscopy, as shown in Fig. 4c and d. The characteristic peak (Fig. 4c) in the FTIR spectrum of pure TiO_2 were observed at 2360 cm^{-1}, which was attributed to vibration of Ti-O-Ti groups. Compared with pure TiO_2, TCF composites appear a narrow weak band at 2210 cm^{-1}, which was assigned to stretching vibration of C≡C, and a broad strong peak at 1689 cm^{-1}, ascribed to stretching vibration of C═O. On the other hand, the absorption peaks around 2210 cm^{-1} and 1689 cm^{-1} was gradually strengthened with the increase of the molar ratio of Fe/Ti, suggesting that carbon layer was successfully *in-situ* generated in the TCF composites, and the chemical bonds were firmly built between TiO_2 shell and carbon layer via the adjacent C═O groups rather than physical adsorption. As shown in Raman spectra (Fig. 4d), pure TiO_2 demonstrated typical four main bands at 141, 394, 513, 635 cm^{-1} due to the Raman active anatase modes $E_g(1)$, $B_{1g}(1)$, $B_{1g}(1)$ and $E_g(3)$ of, respectively [33]. Compared to that of pure TiO_2, TCF composites display similar characteristic Raman bands, and while on increase of molar ratio Fe/Ti from 10% to 25%, the intensity of anatase phase gradually decreased due to the fact that the bond strength of Ti—O was weakened for the strong chemical bond at the interface of TiO_2, carbon layer and $FeTiO_3$. More importantly, the prominent Raman band at 143 cm^{-1} gradually broadened and shifted to a lower wavenumber (blue shift) with the increase molar ratio of Fe/Ti, which might be ascribed to the increasing of lattice disorder resulting from phonon confinement or changes of surface oxygen deficiency [34]. This observation of Raman spectra is supported by the HRTEM, XRD and FTIR results.

To further investigate the constituent components and the chemical bonding states of TCF composites (10%, 15%, 20% and 25%), the as-synthesized samples were characterized by XPS. The full-scanned XPS spectrum of TCF composites (Fig. 5a) mainly exhibits the peaks of Ti $2p_{2/3}$, Ti $2p_{1/2}$, O 1 s, C 1 s and Fe 2p, suggesting that the existence of Ti, O, C and Fe elements in the all TCF composites. The high resolution XPS spectra of Ti 2p from TCF-10% to TCF-25% composites in Fig. 5b presents two peaks at 462.9 eV and 457.4 eV, which originated from the binding energies of Ti $2p_{1/2}$ and Ti $2p_{3/2}$, suggesting the oxidation state Ti^{4+} in TCF composites [6]. In comparison to pure TiO_2 in the standard literature, two peaks of Ti $2p_{1/2}$ and Ti $2p_{3/2}$ gradually shifted towards a lower binding energy values for TCF composites with the increasing of the molar ratio of Fe/Ti due to the strong surface coupling between TiO_2 shell and $FeTiO_3$-embedded carbon layer through the formation of core-shell hollow structure, which induced the possible charge transfer in the TCF composites [35]. As presented in Fig. 5c, the high-resolution XPS spectra of the C1 s shows two bands: one strong peaks at 283.7 eV, which was attributed to C—C binding energies and another weak band at 287.5 eV, which was attributed to C═O binding energies, both of which gradually increased with the increasing of the molar ratio of Fe/

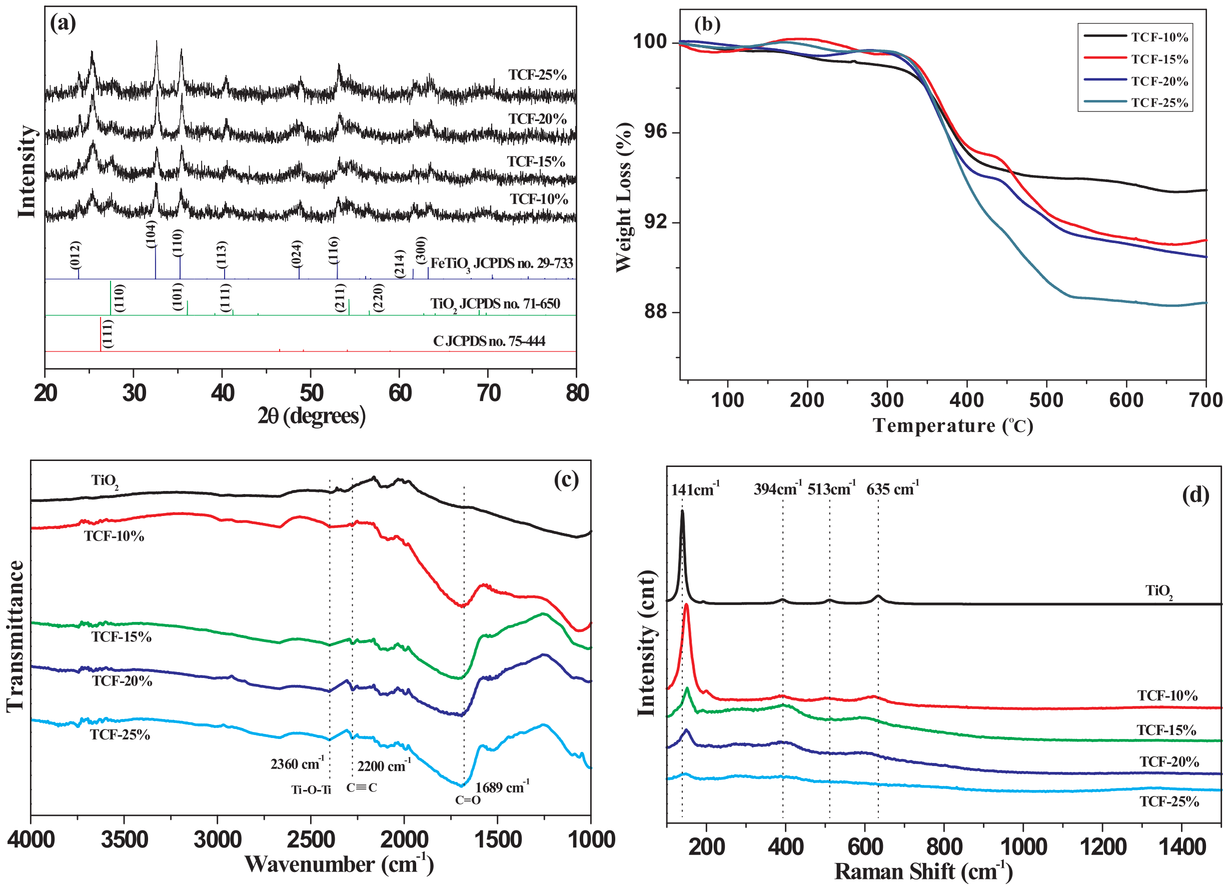

Fig. 4. (a) XRD patterns of TiO_2 nanospheres and TCF nanotubes with the molar ratio of Fe/Ti (10%, 15%, 20% and 25%); (b) TGA diagram of TCF nanotubes composites; (c) FTIR spectra of TiO_2 nanospheres and TCF nanotubes composites; (d) Raman spectra of TiO_2 nanospheres and TCF nanotubes composites.

Ti, indicating that carbon layer thickness was increased. The XPS spectrum of Fe 2p spectrum (Fig. 5d) shows two peaks at 709.5 eV and 722.4 eV, which was assigned to Fe $2p_{3/2}$ and Fe $2p_{1/2}$ binding energies of Fe^{2+}, indicating the presence of $FeTiO_3$ in the TCF composites. All XPS spectra of TCF composites further revealed that with the increasing of molar ratio of Fe/Ti, the peak intensities of C 1 s and Fe 2p gradually increased, while the peak intensity of Ti 2p and O 1 s decreased, suggesting that the thickness of $FeTiO_3$-embedded carbon layer and TiO_2 shell could be controllably tuned within a certain range through the regulating the molar ratio of Fe/Ti, which strengthen the interaction of electronic coupling and facilitate photogenerated electron-hole separation.

Fig. 6a shows the UV–vis diffuse reflectance spectra (DRS) of TiO_2 nanospheres and TCF nanotubes composites. It can be seen that pure TiO_2 nanospheres shows no significant visible light absorption and its absorption band edge was around 390 nm, corresponding to the wide band gap of anatase TiO_2 (3.2 eV). Compared with TiO_2 nanospheres, the absorption spectra of all TCF nanotubes composites appear an obvious broad bands in the UV and visible-light region from 300 to 800 nm. Moreover, the intensity of visible light absorbance gradually increased for TCF nanotubes composites with the increasing of the molar ratio of Fe/Ti in the order of TCF-25% > TCF-20% > TCF-15% > TCF-10%. Therefore, the synergistic effects of TiO_2 shell and $FeTiO_3$-embedded carbon layer play a critical role to harvest visible light energy, which is expected to enhance its full-light-driven photocatalytic activity.

Photoluminescence (PL) measurement is effective method to investigate the separation and transfer efficiency of photogenerated charge carriers in semiconductor [36]. Fig. 6b exhibits the PL spectra of TiO_2 nanospheres and TCF nanotubes composites with the different molar ratio of Fe/Ti at excited wavelength of 320 nm in the range of 400–600 nm. By comparison, TiO_2 and TCF composites present a similar shape and position of the curves and the distinct peak position at about 453, 469, 537 and 574 nm were ascribed to the valance band edge free excitons, surface defects and hole trapped electrons resulting from oxygen vacancy of anatase TiO_2 [37]. The PL emission intensity decreased in the order of TCF-20% < TCF-25% < TCF-15% < TCF-10% < TiO_2, indicating that TCF-20% composites have a relatively lower recombination efficiency of photogenerated electrons and holes, which is often associated with enhanced quantum efficiency. This result indicates that the PL emission intensities of TiO_2 significantly decreased after the tri-coupling with $FeTiO_3$-embedded carbon layer and the well-designed hollow hybrid structure can greatly suppress the recombination of photoinduced charge carriers.

To evaluate the photoelectrochemical (PEC) characteristics of TCF nanotubes composites photoanodes, linear sweep voltammograms (LSV) measurement are performed at a sweep rate of 100 mVs^{-1} in the potential window of -1.0–1.0 V under full spectrum light irradiation (320–2500 nm). As shown in Fig. 7a, the full spectrum light photocurrent response of TiO_2 was very small comparing with TCF composites. For TCF composites, the photocurrent density increased with the increasing of molar ratio Fe/Ti from 10% to 20%, then decreased in 25% and TCF-20% exhibits the biggest positive photocurrent intensity and a maximum negative shift of the onset potential, which is ascribed the optimal synergistic effect by the strong electronic and chemical interaction of TiO_2 shell, carbon layer and $FeTiO_3$ nanopartices. The photocurrent densities of TCF-20% composites at 1 V *vs.* SCE. were determined to 6.03 mA, which is about 40 folds higher than that of TCF-10% composites, indicating that TCF-20% composites effectively improving photoelectron transfer efficiency and reducing the charge

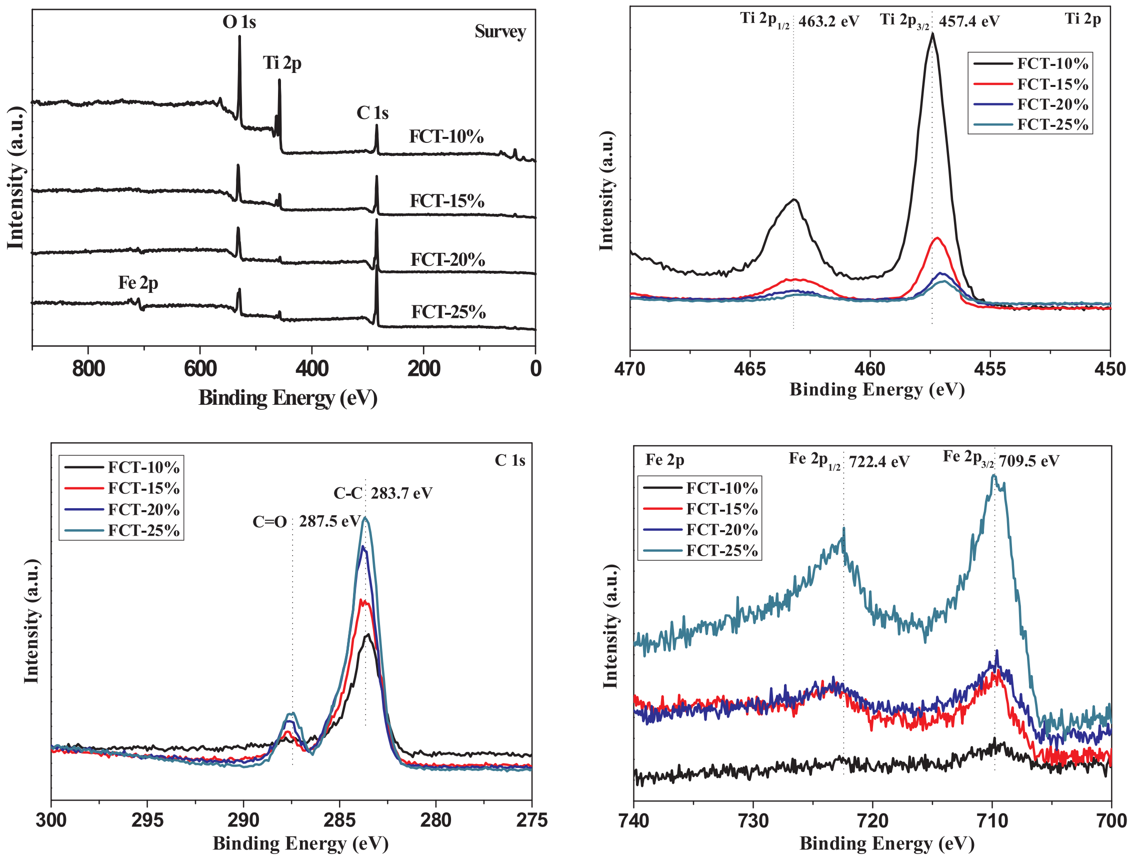

Fig. 5. XPS survey of TCF nanotubes composites with the molar ratio of Fe/Ti (10%, 15%, 20%, 25%): (a) XPS full spectra; (b)Ti 2p; (c) C 1S; (d)Fe 2p.

recombination, shows an enhanced PEC performance. Therefore, above mentioned analysis revealed that TCF composites tremendously displayed the enhanced PEC performance and while the thicker carbon layer has resulted in the longer charge transfer distance, which may impede the transfer of photoelectrons.

To further investigate the separation efficiency of photogenerated electron-hole pairs in as-synthesized TCF composites and TiO_2@$FeTiO_3$-20% nanotubes, the transient photocurrent measurements were tested with switched ON-OFF cycles of full spectrum light illumination. As shown in Fig. 7b, when the TiO_2@$FeTiO_3$-20% nanotubes electrode was under full spectrum light irradiation, there was a little photocurrent density. However, the photocurrent of TCF composites have a continuous increasing trend with the increasing of the molar ratio of Fe/Ti from 10% to 20%, obtaining a highest photocurrent intensity at TCF-20%, and then reduced at TCF-25%. This results further indicate that the existence of middle conductive-layer carbon in the TCF composites can significantly enhance the electron mobility, and however the surplus molar ratio Fe/Ti has resulted in excessive shell thickness of carbon, which may hinder the separation of photoinduced electron-hole pairs and charge transfer in the TCF composites. TCF-20% composites exhibited the highest photocurrent density in all of the samples and reached 2.51 mA cm^{-2}, which is almost 11.3 times larger than that of TCF-10% (*ca.* 0.22 mA cm^{-2}), due to the optimal synergistic effects of TiO_2 shell, the middle conductive shell of carbon and $FeTiO_3$ nanoparticles. This is consistent with the LSV results in Fig. 7a. The result confirms that the quantum efficiency can be tuned by optimizing molar ratio of Fe/Ti and TCF-20% with the appropriate molar ratio of Fe/Ti may achieve more effective charge separation and highly improved

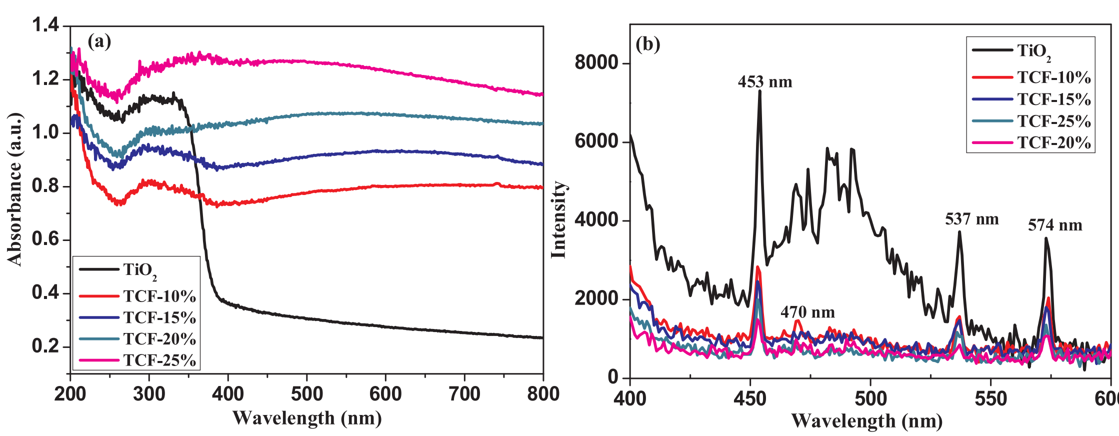

Fig. 6. (a) UV–vis diffuse reflectance spectra of TiO_2 nanospheres and TCF nanotubes with the different molar ratio of Fe/Ti (10%, 15%, 20, 25%); (b) Photoluminescence spectra of TiO_2 nanospheres and TCF nanotubes with the different molar ratio of Fe/Ti (10%, 15%, 20, 25%).

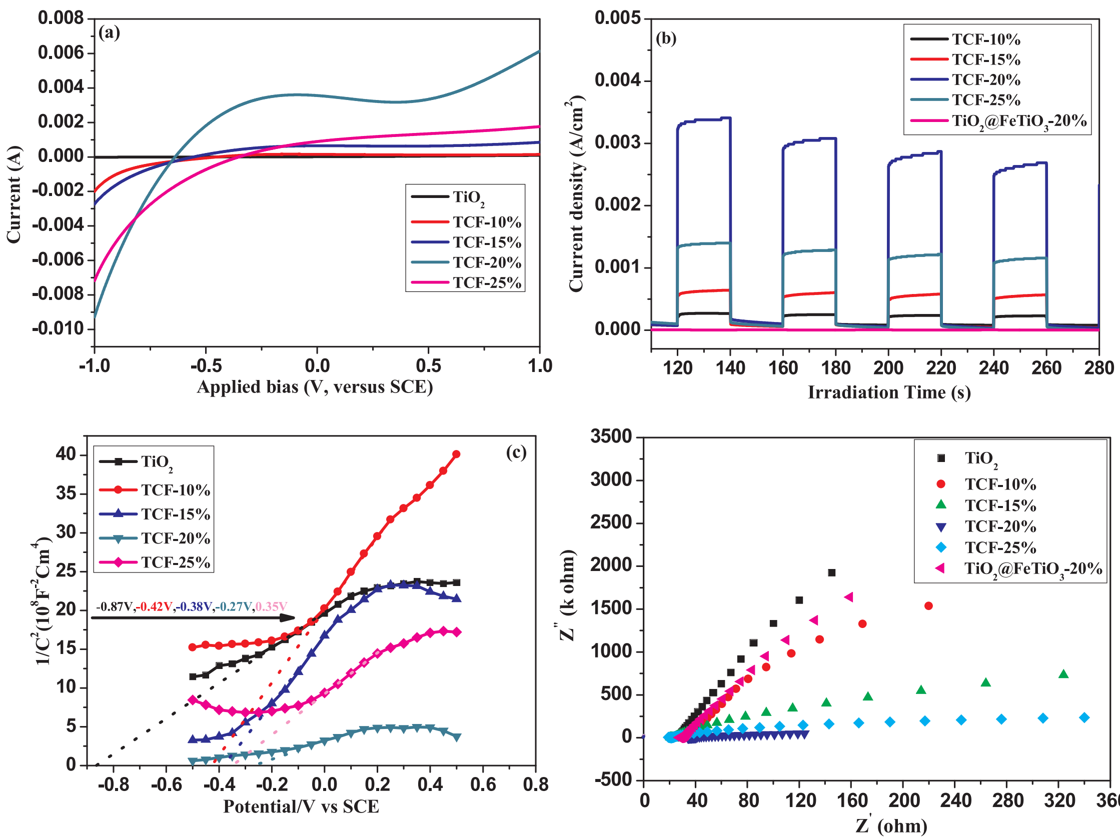

Fig. 7. (a) Linear sweep voltammograms (LSV) of TiO_2 nanospheres and TCF composites with different molar ratio of Fe/Ti (10%, 15%, 20%, 25%); (b) Photocurrent response of TiO_2 nanospheres, TCF composites and TiO_2@$FeTiO_3$-20% nanotubes; (c) Mott-Schottky (MS) plots of TiO_2 nanospheres and TCF composites; (d) Nyquist plots of TiO_2 nanospheres, TCF composites and TiO_2@$FeTiO_3$-20% nanotubes under full spectrum light irradiation.

photocatalytic activity than that of other TCF composites.

In order to investigate the electronic potential of pure TiO_2 and TCF composites, Mott-Schotty analysis was carried out. As shown in Fig. 7c, TiO_2 nanospheres and TCF composites with the positive slope show the n-type semiconductor properties, namely electron as the majority carriers and the value of E_{fb} (flat band potential) by means of extrapolating the extension line to $1/C^2 = 0$, was determined as -0.87 V, -0.42 V, -0.38 V, -0.27 V and -0.35 V for TiO_2 nanospheres, TCF-10%, TCF-15%, TCF-20% and TCF-25%, respectively. In comparison to the flat band potential of TiO_2 nanospheres (-0.87 V), E_{fb} of TCF composites has a more largely positive shift, which effectively improve electron transport by a decrease in the bending of the band edge [36]. According to a linear relationship of $1/C^2$ *vs.* V in the Mott-Schottky equation, TCF-20% composites have a smaller slope in the Mott-Schottky plot than that of other TCF samples, indicating a higher donor density. Furthermore, based on the calculation from the slope of Mott-Schottky plots, it can be speculated that the donor density (N_d) of TCF-20% composites is about 4.17 times higher than that of TCF-10% composites, indicating enhanced electron transfer efficiency due to the optimal tri-coupling effects in the TCF composites system. Electrochemical impedance spectroscopy (EIS) analysis has been utilized to investigate the internal resistance of the charge transportation process in the TCF nanotubes composites system. Fig. 7d shows the Nyquist plots of TiO_2 nanospheres, TCF composites and TiO_2@$FeTiO_3$-20% nanotubes under full spectrum light irradiation, and the less impedance arc represents a faster interfacial charge transfer [38]. As displayed in Fig. 7d, the arc radius of all the TCF composites are obviously smaller than that of radium of TiO_2 nanospheres and TiO_2@$FeTiO_3$ nanotubes indicating that carbon layer in the TCF composites further promote the charge transfer. Moreover, the arc radius of TCF composites gradually decreased with an increasing of the molar ratio of Fe/Ti and TCF-20% composites exhibit the smallest arc radius, then the arc radius of TCF-25% increased, indicating that TCF-20% composites have an optimal matchable interaction in three-component TCF composites, which achieve the fastest charge transfer efficiency among the samples.

This is well known that phenol has been widely used in many industrial fields because of its commercial importance and, while it has been resulted in serious environmental pollution [39]. Therefore, in this research, phenol is selected as the target pollutant models. In comparison to electrocatalysis assisted photocatalytic process, the PC, EC and PEC degradation of phenol solution was investigated by using TCF composites and TiO_2@$FeTiO_3$-20% nanotubes in the ITO films under full spectrum light irradiation with an applied positive bias of 1.5 V vs. SCE. As shown in Fig. 8a in the PC process, the direct photolysis of phenol is almost ignored under full spectrum light irradiation because of its stable molecular and dark absorption is difficult to occur on the surface of TCF composites films. Moreover, TCF composites and TiO_2@$FeTiO_3$-20% photoanodes exhibit the poor photocatalytic activity in the degradation of phenol and degradation rate was around 9.50% for TCF-20% composites photoanode after 180 min of full spectrum light irradiation time, which is higher than that of other TCF composites and TiO_2@$FeTiO_3$-20% films. It can be seen from Fig. 8b that the TiO_2@$FeTiO_3$-20% films have a certain electrocatalytic degradation activity to phenol and the degradation rate constant is 0.061 h^{-1}. However, TCF composites exhibit a better electrocatalytic activity than that of TiO_2@$FeTiO_3$-20% films and the degradation rate constant has gradually increased with an increasing of molar ratio of Fe/Ti, achieving a maximum kinetic constant (0.124 h^{-1}) at TCF-20% film and then decreased at TCF-25% film (0.108 h^{-1}). It is obvious in Fig. 8c that all the TCF composites and TiO_2@$FeTiO_3$-20% photoanodes show better PEC degradation rate under full spectrum light irradiation than corresponding EC process. The PEC degradation rate constants decreased in the

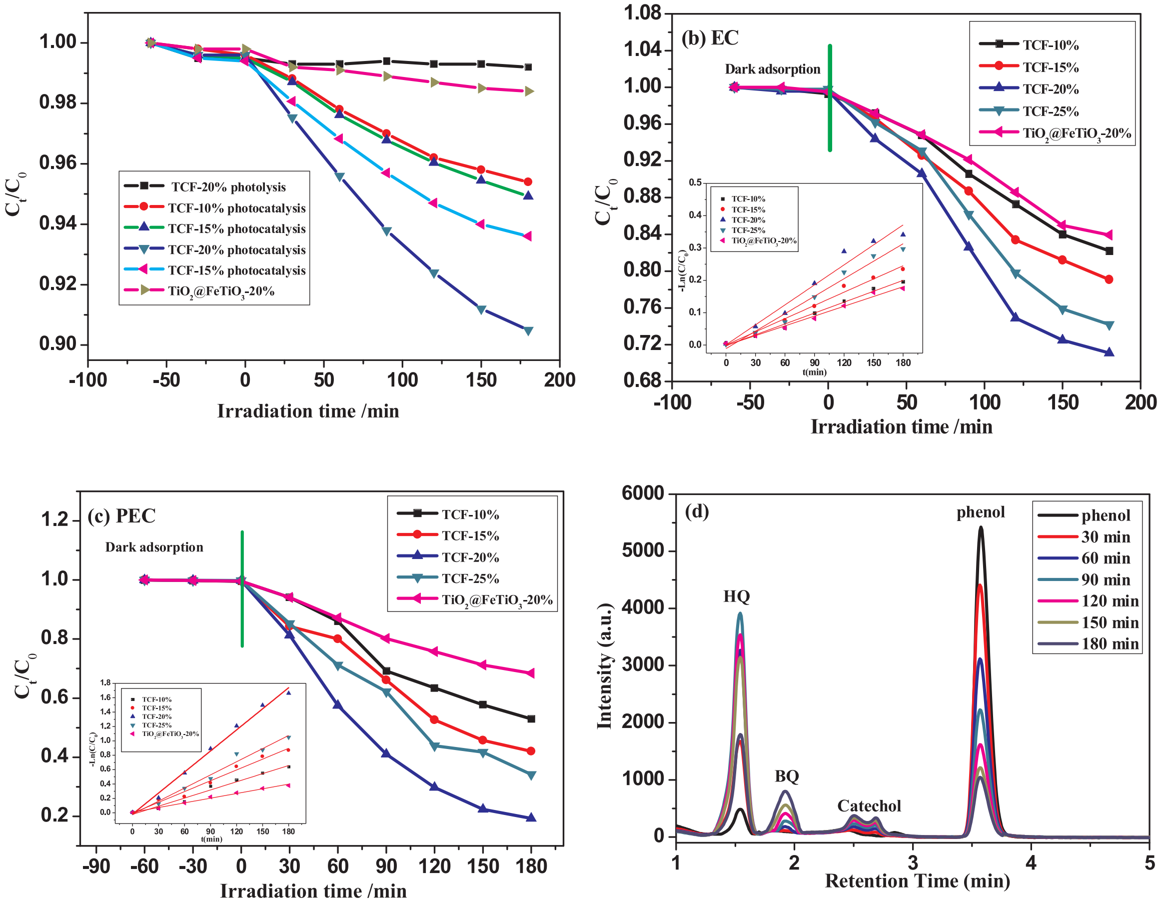

Fig. 8. (a) Phenol degradation in direct photolysis and photocatalysis using TCF composites with the molar ratio Fe/Ti (10%, 15%, 20%, 25%) and $TiO_2@FeTiO_3$-20% nanotubes photoanodes under full spectrum light irradiation; (b) EC degradation of phenol over TCF composites and $TiO_2@FeTiO_3$-20% nanotubes films at an applied potential of 1.5 V; (c) PEC degradation of phenol over TCF composites and $TiO_2@FeTiO_3$-20% nanotubes photoanodes at an applied potential of 1.5 V under full spectrum light irradiation; (d) HPLC graphs of PEC degradation of phenol at different reaction times using TCF-20% photoanode.

following order: TCF-20% > TCF-25% > TCF-15% > TCF-10% > $TiO_2@FeTiO_3$-20%. It is clear that TCF-20% photoanode exhibits a higher full spectrum light PEC activity of degradation phenol in comparison to $TiO_2@FeTiO_3$-20% and other samples, and the degradation rate constant is 0.586 h^{-1}, which is up to 4.5 times faster than that of PEC degradation rate constant of $TiO_2@FeTiO_3$-20% composites film. According to careful analysis of degradation rate of PC (9.5%), EC (28.9%) and PEC (80.7%) for TCF-20% composites film within 3 h, the obtained experimental data proved that degradation rate of PEC is 2.75 times larger than that of the corresponding sum of both EC and PC process, indicating that PEC process combining the advantages of photocatalysis and electrochemical oxidation, have a significant synergistic effect. As described above-mentioned experimental facts and analysis, the enhanced PEC activity of TCF-20% composites could be ascribed to three vital reasons: Firstly, black carbon layer and highly dispersed $FeTiO_3$ nanoparticles embedded on carbon layer in the TCF composites system can harvest full spectrum light energy and broaden the range of spectral absorption, and thus the increased protons can participate in the degradation reaction; Secondly middle conductive-layer carbon greatly accelerates photoinduced electrons transfer from TiO_2 shells to $FeTiO_3$ nanoparticles because of its high conductive properties and the optimal shell thickness of TCF nanotubes may achieve more effective separation of photoinduced electron-hole pairs due to the optimal matchable interaction in three-component TCF composites; Finally, the applied bias potential further supplied powerful external force to the separation of the photogenerated electron-hole pairs and suppressed the recombination of photogenerated electron-hole pairs in TCF composites system.

The PEC degradation process of phenol and its intermediates using TCF-20% photoanode was investigate by HPLC chromatogram. As shown in Fig. 8d, four main peaks were detected at 1.54 min, 1.92 min, 2.51 min and 3.57 min in the chromatogram spectra, and they are corresponding to hydroquinone (HQ), p-benzoquinone (BQ), catechol and phenol, respectively. The prominent peak of phenol observed at 2.51 min gradually decreases with the PEC degradation time extending, while the peaks of intermediates (p-benzoquinone and catechol) continuously increased within 30–180 min. Furthermore, the peak of HQ become more and more stronger within 30–90 min and then gradually decreased from 120 min to 180 min, suggesting that benzene ring has been broken and converted to small molecular organic acids [30,40]. By comparison, the HPLC chromatogram spectra obtained 180 min shows small amount of HQ, but an increasing amount of BQ which can be totally degraded without producing any further toxic products, but only mineralizing into CO_2 and H_2O. From the species and amount of intermediates, it can be inferred that TCF-20% photoanode has a certain ability of mineralization. The phenol oxidation in the PEC degradation process was investigated by total organic carbon (TOC) analyzer. As shown in Fig. S7, the degradation rate of TCF-20% photoanode film has been obtained 80.7% during 180 min, while the mineralization percentage of phenol was about 61.3%. In other words, the mineralization ability was distinctly worse than that of PEC degradation ability for TCF-20% photoanode, indicating that the total mineralization of intermediates (HQ, BQ and catechol) would need a certain time of PEC degradation.

To identify the possible mechanism for the PEC degradation of phenol, electron spin resonance (ESR) spin-trap technique over TCF-

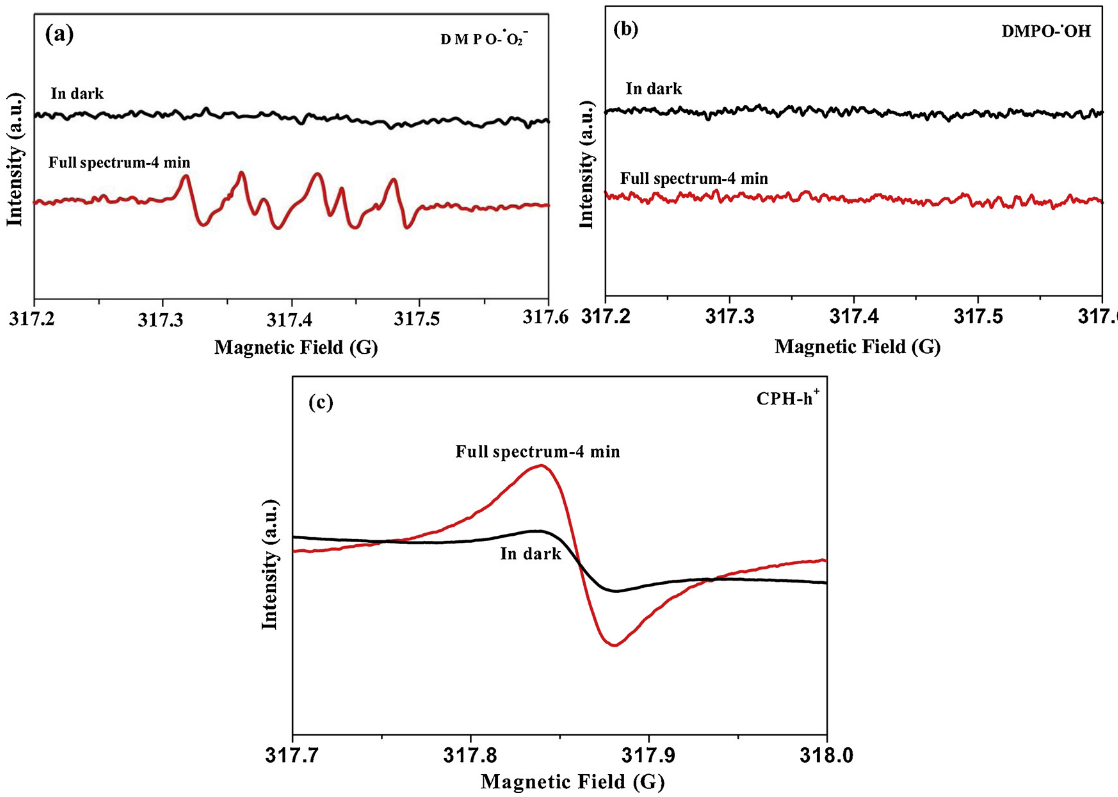

Fig. 9. ESR spectra of TCF-20% composites (a) DMPO-·O_2^- in methanol dispersion; (b) DMPO-·OH in the water solution; (c) CPH-h^+ (0.04 mM CPH).

20% composites was utilized to investigate the main active species such as superoxide radical species (˙O_2^-), hydroxyl radicals (˙OH) and holes (h^+) under full spectrum light irradiation. As shown in Fig. 9a, there is no signals of DMPO-˙O_2^- in dark, while the signals of DMPO-˙O_2^- appears in methanol after full spectrum light irradiation for 4 min, which means to generate a large amount of ˙O_2^- radicals by reduction of O_2 via the separated one electron. Moreover, the signals of DMPO-˙O_2^- has yielded some split peaks due to the signal response of DMPOX for DMPO directly oxidized by holes [31]. Meanwhile, no signals of DMPO-˙OH adduct (Fig. 9b) were detected either in dark or under full spectrum light irradiation, indicating that holes cannot directly oxidize H_2O molecules to form ˙OH because of its low valence band maximum (VBM) potential for TCF-20% composites. Besides, the characteristic signals of CPH-h^+ was also generated during the full spectrum light irradiation (Fig. 9c). From ESR results, it can be concluded that the active species of photoinduced ˙O_2^- and h^+ are generated on the TCF-20% composites under full spectrum light irradiation and they also play a decisive role of predominant oxidative species in the mineralization of phenol.

Base on the above experimental data and previous literatures [28,31,41], Fig. 10 presents the possible PEC mechanism for the degradation of phenol on the TCF composites under full spectrum light irradiation, which involves special hollow needle-like framework induced the enhancement of PEC activity and synergistic effects between electrocatalysis and photocatalysis. Firstly, the delicate architecture of TiO_2 shell and $FeTiO_3$-embedded carbon layer in the TCF composites play a vital role as photosensitizer, which can harvest full spectrum light energy and significantly enhance solar utilization efficiency. Secondly, TCF ternary composites have matched energy band levels and form a typical Type-B heterojunction structures with an internal stepwise electric field at the intimate interface of TiO_2 shell and $FeTiO_3$ nanoparticles embedded at carbon layer because the valence band (VB) level of $FeTiO_3$ is +2.6 V (*vs.* NHE) that approaches the VB position of TiO_2 (+2.7 V *vs.* NHE), while its conduction band is 0 V, which is more positive than that of TiO_2 (-0.5 V *vs.* NHE) [26]. The photoinduced electrons in the VB of both $FeTiO_3$ nanoparticle and TiO_2 shell are excited to their corresponding CB under full spectrum light irradiation and then electrons transfer from the CB of TiO_2 to CB of $FeTiO_3$ through the interface of the intermediate layer of carbon with high conductivity due to its more positive CB level than $FeTiO_3$, it results in the formation of an internal electric field, which can effectively assist the separation and migration of phtotindeced electron-hole charges [27,42]. In our case, the conductive intermediate layer of carbon in the TCF composites play a vital role as accelerated electron channel between TiO_2 shell and $FeTiO_3$ nanoparticles, and increase transmission efficiency of photogenerated electrons from TiO_2 shell to $FeTiO_3$ nanoparticles [43]. On the contrary, the holes (h^+) located at the VB of $FeTiO_3$ are facilitated to transfer to the VB of TiO_2 for the VB position of $FeTiO_3$ being close to that of TiO_2, which has been proved by the previous reports [26–28,44]. Finally, electrocatalysis assisted photocatalysis has further boosted transfer efficiency of photoinduced electrons. Electrons on the $FeTiO_3$ nanoparticles would quickly migrate to that of TCF photoanode under the driving force of an applied potentials and subsequently transferred to counter Pt wire cathode through the external circuit [30]. The electrons on the Pt cathode and TCF photoanode are more negative than that of E(O_2/O_2^-) (-0.33 eV *vs.* NHE) and they would react with dissolved molecular O_2 to generate ˙O_2^- radicals and H_2O_2. Moreover, because the E_{CB} of TiO_2 (-0.5 V *vs.* NHE) was negative than E(OH-/˙OH) (+ 1.99 eV *vs.* NHE) and E(H_2O/˙OH) (+ 2.27 eV *vs.* NHE), accumulated holes in the VB of TiO_2 could not react with H_2O to generate ˙OH [45]. This results have been proved ESR data in Fig. 9. Therefore, the dominant active species of ˙O_2^- and holes as a strong oxidant, take part in the degradation of the phenol and enhanced the mineralization rate. Moreover, the molar ratio of Fe/Ti has a significant effect on shell thickness of TCF composites and PEC activity. Among the samples, TCF-20% with shell thickness of 22 nm exhibit the best PEC activity due to an optimal matchable interaction in ternary TCF composites, which achieve the fastest charge transfer efficiency than other samples. When

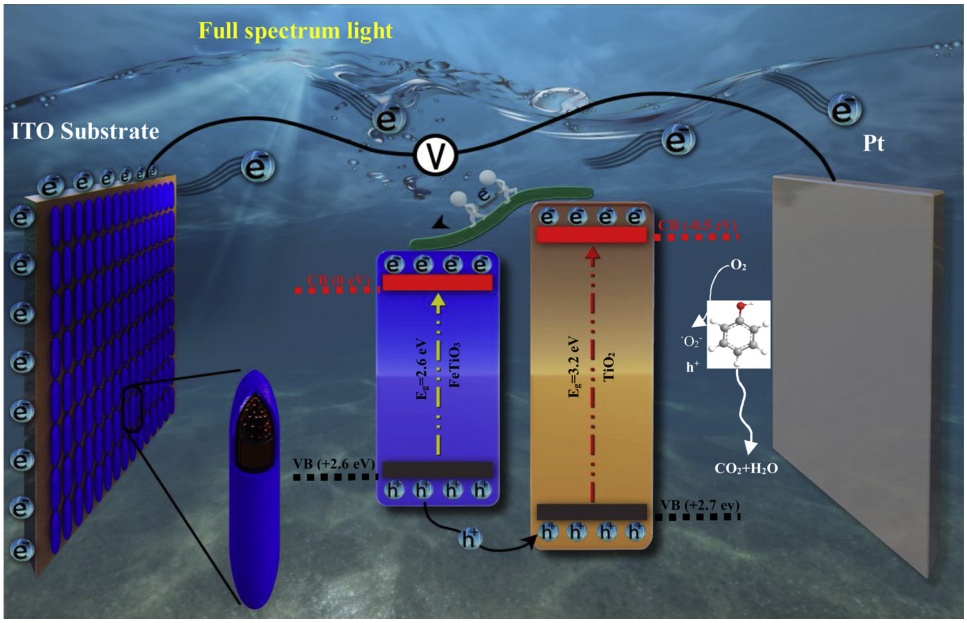

Fig. 10. Schematic illustration of PEC degradation of phenol using TCF-20% as photoanode and Pt as the counter electrode under full spectrum light irradiation.

further increasing of the molar ratio of Fe/Ti, the thicker shell thickness of TCF composites has resulted in the longer charge transfer distance, which may deteriorate PEC activity. In addition, the recycling experiments for TCF-20% was shown in Fig. S8. The PEC activity of TCF-20% after 5 cycles does not exhibit an obvious decrease, indicating excellent cyclic stability of TCF composites.

4. Conclusion

In summary, we have successfully developed a MOF-derived strategy to fabricate the ternary TiO_2@C/$FeTiO_3$ composites involving Fe-MOFs nanorods as sacrificial template and subsequent the carbonization of inorganic-organic core-shell TiO_2@Fe-MOFs at 600 ℃ in a N_2 atmosphere. The shell thickness of TCF hollow nanotubes can be controllably tuned within a certain range from 20 to 25 nm by changing the molar ratio of Fe/Ti in the reaction system, indicating that it creates opportunities to regulate structural features related catalytic properties. Among all of samples with the different molar ratio Fe/Ti, TCF-20% photoanode exhibited a higher full spectrum light PEC activity and the degradation rate constant is 0.586 h^{-1} for the degradation of phenol, which is 2.75 times larger than that of the corresponding sum of both EC and PC process. This highly PEC performance of TCF-20% composites could be attributed to triple synergistic effects of full spectrum light absorption, the hollow structure with middle conductive-layer carbon and matched energy band levels, and electro-oxidation assisted photocatalysis.

Acknowledgements

The authors gratefully acknowledge the financial support of National Natural Science Foundation of China (Grant NO. 21806065, 21777080, 201437003 and 21621003), National Basic Research Program of China (Grant NO. 2013CB632403), Beijing Municipal Science and Technology Project (Grant NO. Z181100005118007) and Collaborative Innovation Center for Regional Environmental Quality, Natural Science Foundation of Liaoning (Grant NO. 2015020577), Young Talents Foundation of University of Science and Technology Liaoning (Grant NO. 2015RC10, 601011507-24), the Scientific Research Foundation of the Educational Department of Liaoning Province (Grant NO. 2017LNQN10).

Appendix A. Supplementary data

Supplementary material related to this article can be found, in the online version, at doi:https://doi.org/10.1016/j.apcatb.2019.03.002.

References

[1] X. Xu, J. Liu, Z. Liu, J. Shen, R. Hu, J. Liu, L. Ouyang, L. Zhang, M. Zhu, Robust pitaya-structured pyrite as high energy density cathode for high-rate lithium batteries, ACS Nano 11 (2017) 9033–9040.

[2] X. Xu, J. Liu, J. Liu, L. Ouyang, R. Hu, H. Wang, L. Yang, M. Zhu, A general Metal-Organic Framework (MOF)-derived selenidation strategy for in situ carbon-encapsulated metal selenides as high-rate anodes for Na-Ion batteries, Adv. Funct. Mater. 28 (2018) 1707573.

[3] J. Wang, W. Shi, D. Liu, Z. Zhang, Y. Zhu, D. Wang, Supramolecular organic nanofibers with highly efficient and stable visible light photooxidation performance, Appl. Catal. B Environ. 202 (2017) 289–297.

[4] Z. Wei, J. Hu, K. Zhu, W. Wei, X. Ma, Y. Zhu, Self-assembled polymer phenylethnylcopper nanowires for photoelectrochemical and photocatalytic performance under visible light, Appl. Catal. B Environ. 226 (2018) 616–623.

[5] Y. Yang, P. Gao, Y. Wang, L. Sha, X. Ren, J. Zhang, P. Yang, T. Wu, Y. Chen, X. Li, A simple and efficient hydrogen production-storage hybrid system (Co/TiO_2) for synchronized hydrogen photogeneration with uptake, J. Mater. Chem. A 5 (2017) 9198–9203.

[6] D. Yang, T. Wu, C. Chen, W. Guo, H. Liu, B. Han, The highly selective aerobic oxidation of cyclohexane to cyclohexanone and cyclohexanol over V_2O_5@TiO_2 under simulated solar light irradiation, Green Chem. 19 (2017) 311–318.

[7] Z. Wu, C. Gong, J. Yu, L. Sun, W. Xiao, C. Lin, Enhanced visible light photoelectrocatalytic activity over $Cu_xZn_{1-x}In_2S_4$@TiO_2 nanotube array hetero-structures, J. Mater. Chem. A 5 (2017) 1292–1299.

[8] F.H. Wei, D. Chen, Z. Liang, S.Q. Zhao, Y. Luo, Preparation of Fe-MOFs by microwave-assisted ball milling for reducing Cr(vi) in wastewater, Dalton Trans. 46 (2017) 16525–16531.

[9] B. Ma, P.Y. Guan, Q.Y. Li, M. Zhang, S.Q. Zang, MOF-derived flower-like MoS_2@TiO_2 nanohybrids with enhanced activity for hydrogen evolution, ACS Appl. Mater. Interfaces 8 (2016) 26794–26800.

[10] D. Xie, Y. Ma, Y. Gu, H. Zhou, H. Zhang, G. Wang, Y. Zhang, H. Zhao, Bifunctional NH_2-MIL-88(Fe) metal–organic framework nanooctahedra for highly sensitive detection and efficient removal of arsenate in aqueous media, J. Mater. Chem. A 5 (2017) 23794–23804.

[11] L. Yu, J. Liu, X. Xu, L. Zhang, R. Hu, J. Liu, L. Yang, M. Zhu, Metal-organic framework-derived NiSb alloy embedded in carbon hollow spheres as superior lithium-ion battery anodes, ACS Appl. Mater. Interfaces 9 (2017) 2516–2525.

[12] J. Liu, C. Wu, D. Xiao, P. Kopold, L. Gu, P.A. van Aken, J. Maier, Y. Yu, MOF-derived hollow Co_9S_8 nanoparticles embedded in graphitic carbon nanocages with superior Li-Ion storage, Small 12 (2016) 2354–2364.

[13] G. Huang, F. Zhang, L. Zhang, X. Du, J. Wang, L. Wang, Hierarchical $NiFe2O_4$/$Fe2O_3$ nanotubes derived from metal organic frameworks for superior lithium ion battery anodes, J. Mater. Chem. A 2 (2014) 8048–8053.

[14] F. Zou, X. Hu, Z. Li, L. Qie, C. Hu, R. Zeng, Y. Jiang, Y. Huang, MOF-derived porous $ZnO/ZnFe_2O_4$/C octahedra with hollow interiors for high-rate lithium-ion batteries,

Adv Mater 26 (2014) 6622–6628.
[15] S. Bala, I. Mondal, A. Goswami, U. Pal, R. Mondal, Co-MOF as a sacrificial template: manifesting a new $Co3O_4/TiO_2$ system with a p–n heterojunction for photocatalytic hydrogen evolution, J. Mater. Chem. A 3 (2015) 20288–20296.
[16] L.-L. Ling, W.-J. Liu, S.-Q. Chen, X. Hu, H. Jiang, MOF templated nitrogen doped carbon stabilized Pt–Co bimetallic nanoparticles: low Pt content and robust activity toward electrocatalytic oxygen reduction reaction, ACS Appl. Nano Mater. 1 (2018) 3331–3338.
[17] G. Xia, J. Su, M. Li, P. Jiang, Y. Yang, Q. Chen, A MOF-derived self-template strategy toward cobalt phosphide electrodes with ultralong cycle life and high capacity, J. Mater. Chem. A 5 (2017) 10321–10327.
[18] Y. Su, D. Ao, H. Liu, Y. Wang, MOF-derived yolk–shell CdS microcubes with enhanced visible-light photocatalytic activity and stability for hydrogen evolution, J. Mater. Chem. A 5 (2017) 8680–8689.
[19] Y. Liu, W. Zhang, S. Li, C. Cui, J. Wu, H. Chen, F. Huo, Designable Yolk–Shell Nanoparticle@MOF Petalous Heterostructures, Chem. Mater. 26 (2014) 1119–1125.
[20] B. Chen, Y. Meng, J. Sha, C. Zhong, W. Hu, N. Zhao, Preparation of MoS_2/TiO_2 based nanocomposites for photocatalysis and rechargeable batteries: progress, challenges, and perspective, Nanoscale 10 (2017) 34–68.
[21] C. Cionti, C. Della Pina, D. Meroni, E. Falletta, S. Ardizzone, Triply green polyaniline: UV irradiation-induced synthesis of highly porous PANI/TiO_2 composite and its application in dye removal, Chem. Commun. (2018).
[22] T. Hiraide, H. Kageyama, Y. Nakagawa, Y. Oaki, H. Imai, UV-induced epitaxial attachment of TiO_2 nanocrystals in molecularly mediated 1D and 2D alignments, Chem. Commun. (Camb.) 52 (2016) 7545–7548.
[23] B. Liu, Y. Xue, J. Zhang, B. Han, J. Zhang, X. Suo, L. Mu, H. Shi, Visible-light-driven TiO_2/Ag_3PO_4 heterostructures with enhanced antifungal activity against agricultural pathogenic fungi Fusarium graminearum and mechanism insight, Environ. Sci. Nano 4 (2017) 255–264.
[24] S.S. Mali, A.I. Inamdar, H. Im, S.E. Shim, C.K. Hong, Correction: Efficient planar n-i-p type heterojunction flexible perovskite solar cells with sputtered TiO_2 electron transporting layers, Nanoscale 9 (2017) 3655.
[25] H. Zhu, Y. Hu, K. Zhu, S.C. Yan, L. Lu, M. Zhao, H. Fu, Z. Li, Z. Zou, Galvanic cell reaction driven electrochemically doping of TiO_2 nanotube photoanodes for enhanced charge separation, Chem. Commun. (2018).
[26] B. Gao, Y.J. Kim, A.K. Chakraborty, W.I. Lee, Efficient decomposition of organic compounds with $FeTiO_3/TiO_2$ heterojunction under visible light irradiation, Appl. Catal. B Environ. 83 (2008) 202–207.
[27] T. Han, Y. Chen, G. Tian, J.Q. Wang, Z. Ren, W. Zhou, H. Fu, Hierarchical $FeTiO_3$-TiO_2 hollow spheres for efficient simulated sunlight-driven water oxidation, Nanoscale 7 (2015) 15924–15934.
[28] Q.D. Truong, J.-Y. Liu, C.-C. Chung, Y.-C. Ling, Photocatalytic reduction of CO_2 on $FeTiO_3/TiO_2$ photocatalyst, Catal. Commun. 19 (2012) 85–89.
[29] W. Cho, S. Park, M. Oh, Coordination polymer nanorods of Fe-MIL-88B and their utilization for selective preparation of hematite and magnetite nanorods, Chem. Commun. (Camb.) 47 (2011) 4138–4140.
[30] F. Liang, Y. Zhu, Enhancement of mineralization ability for phenol via synergetic effect of photoelectrocatalysis of g-C_3N_4 film, Appl. Catal. B Environ. 180 (2016) 324–329.
[31] J. Wang, Z. Yang, X. Gao, W. Yao, W. Wei, X. Chen, R. Zong, Y. Zhu, Core-shell g-C_3N_4@ZnO composites as photoanodes with double synergistic effects for enhanced visible-light photoelectrocatalytic activities, Appl. Catal. B Environ. 217 (2017) 169–180.
[32] L. Yu, J. Liu, X. Xu, L. Zhang, R. Hu, J. Liu, L. Ouyang, L. Yang, M. Zhu, Ilmenite nanotubes for high stability and high rate sodium-ion battery anodes, ACS Nano 11 (2017) 5120–5129.
[33] M. Long, Y. Qin, C. Chen, X. Guo, B. Tan, W. Cai, Origin of Visible Light Photoactivity of Reduced Graphene Oxide/TiO_2 by in Situ Hydrothermal Growth of Undergrown TiO_2 with Graphene Oxide, J. Phys. Chem. C 117 (2013) 16734–16741.
[34] G. Liu, L.-C. Yin, J. Wang, P. Niu, C. Zhen, Y. Xie, H.-M. Cheng, A red anatase TiO_2 photocatalyst for solar energy conversion, Energy Environ. Sci. 5 (2012) 9603.
[35] S. Yan, S. Ouyang, H. Xu, M. Zhao, X. Zhang, J. Ye, Co-ZIF-9/TiO_2 nanostructure for superior CO_2 photoreduction activity, J. Mater. Chem. A 4 (2016) 15126–15133.
[36] F. Ning, M. Shao, S. Xu, Y. Fu, R. Zhang, M. Wei, D.G. Evans, X. Duan, TiO_2/graphene/NiFe-layered double hydroxide nanorod array photoanodes for efficient photoelectrochemical water splitting, Energy Environ. Sci. 9 (2016) 2633–2643.
[37] J. Hu, Q. Liu, H. Zhang, C.-D. Chen, Y. Liang, R.-G. Du, C.-J. Lin, Facile ultrasonic deposition of SnO_2 nanoparticles on TiO_2 nanotube films for enhanced photoelectrochemical performances, J. Mater. Chem. A 3 (2015) 22605–22613.
[38] J. Wang, W. Jiang, D. Liu, Z. Wei, Y. Zhu, Photocatalytic performance enhanced via surface bismuth vacancy of $Bi_6S_2O_{15}$ core/shell nanowires, Appl. Catal. B Environ. 176-177 (2015) 306–314.
[39] Z. Zhang, J. Wang, D. Liu, W. Luo, M. Zhang, W. Jiang, Y. Zhu, Highly Efficient Organic Photocatalyst with Full Visible Light Spectrum through π–π Stacking of TCNQ–PTCDI, ACS Appl. Mater. Interfaces 8 (2016) 30225–30231.
[40] W. Jiang, M. Zhang, J. Wang, Y. Liu, Y. Zhu, Dramatic visible activity in phenol degradation of TCNQ@TiO_2 photocatalyst with core–shell structure, Appl. Catal. B Environ. 160-161 (2014) 44–50.
[41] Y. Zhang, B. Tang, Z. Wu, H. Shi, Y. Zhang, G. Zhao, Glucose oxidation over ultrathin carbon-coated perovskite modified TiO_2 nanotube photonic crystals with high-efficiency electron generation and transfer for photoelectrocatalytic hydrogen production, Green Chem. 18 (2016) 2424–2434.
[42] M. Zhou, S. Wang, P. Yang, C. Huang, X. Wang, Boron Carbon Nitride Semiconductors Decorated with CdS Nanoparticles for Photocatalytic Reduction of CO_2, ACS Catal. 8 (2018) 4928–4936.
[43] Y. Wu, J. Ward-Bond, D. Li, S. Zhang, J. Shi, Z. Jiang, g-C_3N_4@α-Fe_2O_3/C Photocatalysts: Synergistically Intensified Charge Generation and Charge Transfer for NADH Regeneration, ACS Catal. 8 (2018) 5664–5674.
[44] Y.J. Kim, B. Gao, S.Y. Han, M.H. Jung, A.K. Chakraborty, T. Ko, C. Lee, W.I. Lee, Heterojunction of $FeTiO_3$Nanodisc and TiO_2 Nanoparticles for a Novel Visible Light Photocatalyst, J. Phys. Chem. C 113 (2009) 19179–19184.
[45] S. Sun, W. Wang, L. Zhang, Efficient Contaminant Removal by Bi_2WO_6Films with Nanoleaflike Structures through a Photoelectrocatalytic Process, J. Phys. Chem. C 116 (2012) 19413–19418.